View metadata, citation and similar papers at core.ac.uk

brought to you by CORE

provided by Kanazawa University Repository for Academic Resources

Streptavidin 2D crystal substrates for visualizing biomolecular processes by atomic force microscopy

著者	Yamamoto Daisuke, Nagura Naoki, Omote Saeko, Taniguchi Masaaki, Ando Toshio
journal or publication title	Biophysical Journal
volume	97
number	8
page range	2358-2367
year	2009-10-21
URL	http://hdl.handle.net/2297/19811

doi: 10.1016/j.bpj.2009.07.046

Streptavidin 2D crystal substrates for visualizing biomolecular processes by atomic force microscopy

Daisuke Yamamoto,[†‡] Naoki Nagura,[†] Saeko Omote,[†] Masaaki Taniguchi,[†] and Toshio Ando[†‡]*

[†]Department of Physics, Kanazawa University, Kakuma-machi, Kanazawa 920-1192, Japan;
[‡]Core Research for Evolutional Science and Technology of the Japan Science and Technology Agency, Sanban-cho, Chiyoda-ku, Tokyo 102-0075, Japan

*Correspondence: tando@kenroku.kanazawa-u.ac.jp

Running title:
Streptavidin substrata for dynamic AFM

Keywords:
AFM, high-speed AFM, microscopy, substratum, immobilization, imaging

Current email addresses of authors:
D. Yamamoto: yamadai@kenroku.kanazawa-u.ac.jp
N. Nagura: n_nagura@yahoo.co.jp
S. Omote: somoten@yahoo.co.jp
M. Taniguchi: taniguch@kenroku.kanazawa-u.ac.jp
T. Ando: tando@kenroku.kanazawa-u.ac.jp

Abstract

Flat substrate surfaces are a key to successful imaging of biological macromolecules by atomic force microscopy (AFM). Although suitable substrate surfaces have been prepared for still imaging of immobilized molecules, more suitable surfaces have recently been required for dynamic imaging to accompany the progress of the scan speed of AFM. In fact, the state-of-the-art high-speed AFM has achieved temporal resolution of 30 ms, a capacity allowing us to trace molecular processes played by biological macromolecules. Here, we characterize three types of streptavidin two-dimensional crystals as substrates regarding surface roughness, uniformity, stability and resistance to non-specific protein adsorption. The crystal surfaces are commonly resistant to non-specific protein adsorption but exhibit differences in the other properties to some extent. Although the differences are necessary to be considered in their choice, all the crystal surfaces are usefully applicable to dynamic AFM imaging, which is demonstrated by the observation of calcium-induced changes in calmodulin, GroES binding to GroEL, and actin polymerization on the surfaces.

INTRODUCTION

Atomic force microscopy (AFM) (1) has become a powerful tool for high-resolution visualization of biological samples in aqueous solutions (2–4). Immobilization of biological molecules onto a planar support is prerequisite for the imaging, and therefore, selecting or preparing appropriate substrates is a key to successful imaging. Thus far, a number of immobilization methods have been developed to this end (5–7). Bare mica surface has been frequently used for reproducible imaging of biological samples because it is atomically flat over a wide area and many proteins attach to the surface under buffer solutions. However, because of the electrostatic adsorption, its attachment is often weak and selective attachment in controlled orientation cannot be achieved, except for rare cases. For the firm attachment, chemisorption of biomolecules onto self-assembled monolayers of molecules terminated with chemically reactive groups has been used (8, 9). This immobilization can avoid displacement of biomolecules by a scanning tip. These methods for sample attachment have contributed to the success of still imaging and slow time-lapse imaging (10–13) of biological samples.

Recent advent of high-speed AFM expands the usefulness of AFM for biological research (14, 15). Its maximum imaging rate of 33 frames/s enables direct imaging of biomolecular processes in real time. However, for dynamic AFM imaging of molecular

processes, previously used substrate surfaces are often useless. Biomolecular processes often contain dynamic interactions between molecules. When all molecules are attached to a surface, they have almost no chance to interact with each other. In addition to generally required conditions for the surfaces such as (i) small roughness for identifying the molecules of interest and (ii) a high affinity for the sample, dynamic AFM imaging requires several conditions such as (iii) selective attachment of a specific component in a multi-component sample, (iv) controlled orientation of immobilized molecule, and (v) no perturbation to the biological function of the sample (i.e., absence of nonspecific interactions).

In a pioneering study (16), streptavidin two-dimensional (2D) crystals formed on biotin-containing planar lipid layers (17-20) was imaged by AFM, and their use for biomolecule attachment in AFM studies was proposed. Here, we examined whether the surfaces of streptavidin 2D crystals can fulfill the above-mentioned requirements. Streptavidin is comprised of four identical subunits, each of which specifically binds to one biotin molecule with a strong affinity ($Ka \approx 10^{13}$ M^{-1}) (21). In the 2D crystals, the two biotin binding sites face the free solution, and therefore, can bind to biotinylated samples to be imaged (18, 20). Since biotinylated Ni-NTA is commercially available, the surface also can immobilize his-tag conjugated recombinant proteins without lateral diffusion (note that his-tag conjugated proteins can directly be attached to a Ni-NTA containing lipid bilayer surface but lateral diffusion occurs because of fluidity of the lipid bilayer). Importantly, streptavidin is resistant to nonspecific binding to many proteins (21), which possibly guarantees the surface-bound proteins against disfunction (22).

On biotinylated planar lipid layers, streptavidin self-assembles into three distinct crystalline arrangements (type 1-3 with $P2$ symmetry), depending on the crystallization conditions such as pH (23) and ionic strength (24). Here, we characterize these different 2D crystals taking into consideration the stability, degree of order, surface roughness, and nonspecific binding. Although the surfaces of these crystals satisfy the required conditions for dynamic imaging of molecular processes, our characterization results indicate that it would be better to consider their different properties depending on the sample to be imaged.

Using high-speed AFM, we demonstrate the applicability of these crystal surfaces to dynamic AFM imaging by observing three different samples. For immobilized calmodulin (CaM), its structural changes upon calcium binding was detected. GroEL was immobilized in a controlled orientation (i.e., side-on orientation) by introducing biotin at the outer surface of the equatorial domain of GroEL. Using this orientation in which both ends of GroEL double rings are accessible to GroES, binding of GroES to GroEL was visualized. The process of actin plolymerization was also visualized. Thus, the streptavidin 2D crystals are shown to be a useful tool for high-speed AFM imaging of biomolecular processes.

MATERIALS AND METHODS

Materials

We obtained following materials and used without further purification; streptavidin, Wako Pure Chemical (Osaka, Japan); bovine brain CaM, Calbiochem (Darmstadt, Germany); lipids, Avanti Polar Lipids (Alabaster, AL); biotin-$(AC_5)_2$-sulfo-osu and biotin-$PEAC_5$-maleimide, Dojindo Laboratories (Kumamoto, Japan); Cy3-osu, GE Helthcare (Buckinghamshire, UK); phalloidin, Invitrogen (Carlsbad, CA). Coverslips and natural muscovite mica were purchased from Matsunami (Osaka, Japan) and Nilaco (Tokyo, Japan), respectively.

Coverslips

Coverslips were washed for 30 min with detergent in an ultrasonic bath, and then boiled in H_2SO_4/H_2O_2 (80:20, v/v) to remove hydrocarbon contaminants. After rinsing with MilliQ water, the coverslips were immersed in 6 M KOH for 12 h. Subsequently, the cleaned coverslips were sonicated in MilliQ water.

Preparation of streptavidin 2D crystals

For the measurement by total internal reflection fluorescence microscopy (TIRFM), coverslips are used as the solid support for biotinylated lipid bilayers; a flow cell was built using two coverslips (24 × 36 mm^2 and 18 × 18 mm^2) between which a space was created by two strips of double-sided sticky tape so that a channel for injecting samples and buffer solutions was formed at the center. For AFM imaging, mica (1 mm diameter) or coverslip (2×2 mm^2) was used as the solid supports. Streptavidin 2D crystals were formed on supported biotin-containing lipid bilayers as described (25). Briefly, a supported biotin-containing lipid bilayer was first obtained by applying small unilamellar vesicles (0.125 mM) of lipids to a solid support. The lipid compositions were dioleoylphosphatidylcholine (DOPC), dioleoylphosphatidylserine (DOPS) and 1,2-dioleoyl-*sn*-glycero-3-phosphoethanolamine-*N*-(cap biotinyl) (biotinylated lipid) at 7:2:1 (w/w). After washing out the excess lipids with a crystallization buffer solution, a 0.1–0.2 mg/ml streptavidin solution was placed on the biotinylated lipid bilayer and incubated at room temperature in a sealed container. The crystallization buffers used were 10 mM HEPES, 150 mM NaCl and 2 mM $CaCl_2$ (pH 7.4) for the type-1 *P*2 crystal, 10 mM MES, 450 mM NaCl and 2 mM $CaCl_2$ (pH 5.8) for the type-2 *P*2 crystal and 10 mM acetate, 450 mM NaCl and 2 mM $CaCl_2$ (pH 4.0) for the type-3 *P*2 crystal. After the incubation for at least 2 h, the excess streptavidin was washed out with the buffer solution used for crystallization. For the chemical fixation of the streptavidin crystals, a 10 mM glutaraldehyde-containing

crystallization solution was applied and incubated for 5 min. The reaction was quenched using 20 mM Tris mixed in the crystallization buffer. To distinguish the crystal types, we here used annotations, type-1, type-2 and type-3. For the type-1 *P*2 crystal, *C*222 has been previously used even in the 2D image (16, 20, 25). Although annotation, *P*1, has been used for the type-3 *P*2 crystal (23, 24), it certainly has *P*2 symmetry because the top view of the surface-attached streptavidin tetramer itself has a two-fold rotation symmetry.

Biological samples

CaM. To prepare biotinylated CaM, CaM was reacted with biotin-$(AC_5)_2$-sulfo-osu as described previously (26). For the fluorescent labeling, non-biotinylated or biotinylated CaM was reacted with Cy3-osu as described (26). The molar ratio of biotin to CaM in the biotinylated CaM was determined to be 0.6 based on the avidin-2-(4'-Hydroxybenzeneazo)benzoic acid (HABA) assay (27). The molar ratio of conjugated Cy3 to CaM was 0.7–1.9 throughout the study. Prior to the immobilization of biotinylated CaM, the streptavidin 2D crystals were washed with buffer A (20 mM imidazole, 100 mM KCl, 2 mM $MgCl_2$, 1 mM EGTA, pH 7.6). To distinguish specific and non-specific binding, 0.1 nM of biotinylated or non-biotinylated Cy3-CaM in buffer A was infused to the flow cell. After incubating for 3 min, the sample was washed with buffer A to remove excess Cy3-CaM. To further examine the nonspecific adsorption, a 100-times higher concentration (i.e., 10 nM) of non-biotinylated Cy3-CaM was infused to the flow cell and then observed by TIRFM. For AFM observations, 200 nM biotinylated or non-labeled CaM in buffer A was deposited onto the streptavidin type-3 *P*2 crystal formed on mica-supported lipid bilayer. After 3 min, the sample was washed with buffer A to remove unattached CaM. The AFM measurements were performed in buffer A in the presence or absence of 2 mM Ca^{2+}.

GroEL and GroEL-GroES complexes. The GroEL D490C mutant was produced by site-directed mutagenesis. D490C GroEL and wild-type GroES were expressed in *Escherichia coli* XL1-Blue and purified as described (28). D490C GroEL was dialyzed against buffer B (50 mM HEPES-KOH, 50 mM KCl, 10 mM $MgCl_2$, pH 7.4) containing 2 mM Tris (2-carboxyethyl) phosphine hydrochloride (TECP) and then biotinylated by the reaction with biotin-$PEAC_5$-maleimide (molar ratio of reagent to subunit equal to 1) for 30 min at 25 ºC. The reaction was quenched with 5 mM DTT. To remove unreacted biotin, the sample was dialyzed against buffer B containing 2 mM DTT. The molar ratio of biotin to GroEL subunit was 0.8. The streptavidin type-1 *P*2 crystal formed on mica-supported lipid bilayer was used as a substrate after fixing with glutaraldehyde. The streptavidin crystal was rinsed with buffer B. For high-speed AFM observation, the biotinylated GroEL was diluted

to 25 nM in buffer B and deposited to the streptavidin crystal. After 3 min, the sample was washed with buffer B to remove unattached GroEL. High-speed AFM measurement of GroEL-GroES complex was performed in buffer B in the presence of 1 μM GroES, 1 mM ADP and 2 mM DTT.

Actin. Actin was purified from rabbit skeletal muscles as described (27). Partially biotinylated F-actin was prepared as follows. G-actin was reacted with biotin-$(AC_5)_2$-sulfo-osu as described (29). The molar ratio of conjugated biotin to G-actin was 2.0. The biotinylated G-actin was copolymerized with non-biotinylated G-actin (1:9 molar ratio) in buffer A containing 0.2 mM ATP, and then stabilized with phalloidin. As a substrate, the streptavidin type-2 *P*2 crystal formed on mica-supported lipid bilayer was used after fixing with glutaraldehyde. The streptavidin crystal was rinsed with buffer A. 1 μM of partially biotinylated F-actin in buffer A was deposited to the 2D crystal. After 3 min, the sample was washed with buffer A to remove excess actin. High-speed AFM visualization of polymerization processes of single actin filaments were performed in buffer A in the presence of 1 μM non-biotinylated G-actin, 0.2 mM ATP and 2 mM DTT.

TIRFM

Fluorescently labeled proteins were illuminated with a diode pumped green laser (532 nm; CrystaLaser, Reno, NV). The fluorescence images were captured at 10 frames/s using an inverted fluorescence microscope (IX71; Olympus, Tokyo, Japan) equipped with a high NA objective lens (100× Apo TIRF NA = 1.49; Nikon, Tokyo, Japan) and a CCD camera (Andor Technology, Belfast, Northern Ireland). The recorded images were averaged over 10 frames.

AFM imaging

For scan sizes ≥ 500 nm, images were recorded with a commercial AFM (Nanoscope IVa; Veeco, Santa Barbara, CA) in the tapping mode, using cantilevers (BioLever mini; Olympus, Tokyo, Japan) with a spring constant of 0.1–0.3 N/m. The cantilever was oscillated at its resonant frequency (approximately 30 kHz in water). For scan sizes < 500 nm, high-speed AFM imaging was carried out in the tapping mode, using our laboratory-built instrument (15) and small cantilevers (Olympus, Tokyo, Japan) with a spring constant of 0.1–0.2 N/m and a resonant frequency of 0.8–1.2 MHz in water, as described previously (25).

RESULTS AND DISCUSSION

Surface homogeneity and topographies of streptavidin 2D crystals

The surface homogeneity and small roughness of streptavidin 2D crystals are important factors for easy identification by AFM of proteins immobilized on these surfaces. We examined these properties by imaging streptavidin 2D crystals by AFM. Fig. 1 shows low magnification AFM images of three types of streptavidin 2D crystals formed on mica-supported lipid bilayers. The crystals showed *P*2 space group symmetry with different vector axes (for the molecular arrangements, see Fig. 3); type-1 (Fig. 1 *A*), type-2 (Fig. 1 *B*) and type-3 (Fig. 1 *C*). Wide areas were covered by ordered crystalline lattices, suitable as substrates for AFM imaging of biological molecules. These crystals were stable over a period at lease more than 12 h.

Although not significant obstacles to practical use, the surface of the type-3 *P*2 crystal contained a number of line defects and cracks (Fig. 1 *C*, *arrowheads*), due to a relatively smaller size of crystalline domains. In the type-1 and type-2 *P*2 crystals, the surfaces were continuous and smooth over a wide area (> 1 μm^2), except for a small number of defects such as (i) large particles (Figs. 1, *A* and *C*, *arrows*) and (ii) non-crystallized region (Fig. 1 *B*, *asterisk*). These imperfections of the crystals are likely to be induced by the instability of lipid bilayers underneath the streptavidin crystals or by not fully optimized crystallization conditions.

AFM images at medium magnification revealed more detailed surface structures (Fig. 2). The type-1 *P*2 crystal (Fig. 2 *A*) and the type-2 *P*2 crystal (Fig. 2 *B*) showed a significantly low density of vacancy defects. In contrast, a significant defects such as point (Fig. 2 *C*, *arrowheads*) and line defects (Fig. 2 *C*, outlined with *dashed lines*) were observed in the type-3 *P*2 crystal. However, these lattice defects cannot be severe obstacles to AFM imaging of proteins immobilized on such surfaces. Proteins immobilized onto crystalline areas always protrude from the crystal surface, whereas the vacancies and line defects can be seen as depressions. Therefore, the proteins attached to the crystal surface are easily identified. Note that as mention later, proteins do not attach at least to the cracks because the exposed surfaces are those of lipid bilayers.

Another type of defect is small particles (Fig. 2, *arrows*). The height of these particles was 3.3 ± 1.3 nm, which is comparable to diameters of many proteins. The similar dimensions might be an obstacle to identifying immobilized proteins by AFM. However, the density of small particles is sufficiently low (1–2 particles per 200 × 200 nm^2) to allow AFM imaging of immobilized proteins on the surfaces. The origin of the small particles is uncertain. One possibility could be misalignments of streptavidin in the crystalline arrays.

The molecular arrangements of streptavidin in the different 2D crystals are clearly identified in the high magnification AFM images (Fig. 3, *top*). The lattice constants obtained from the images are a = 5.8 ± 0.1 nm, b = 5.8 ± 0.2 nm and γ = 89 ± 1 º for the type-1 *P*2

crystal (Fig. 3 *A*), a = 5.8 ± 0.1 nm, b = 11.3 ± 0.1 nm and γ = 102 ± 3 º for the type-2 *P*2 crystal (Fig. 3 *B*) and a = 5.5 ± 0.1 nm, b = 4.6 ± 0.1 nm and γ = 110 ± 2 º for the type-3 *P*2 crystal (Fig. 3 *C*). These values well agree with those obtained in previous studies (18, 30, 31), when the unit cells are consistently selected. The Fourier transformation of the AFM images showed characteristic diffraction patterns for respective streptavidin 2D crystals (Fig. 3, *middle*). The maximum diffraction spots ranging 0.83 – 0.9 nm^{-1} were obtained for all three types of streptavidin 2D crystals, although it does not necessarily represent the spatial resolution of the images (32).

The small roughness of the crystal surfaces is an important factor when they are served as substrate surfaces for AFM imaging. The cross-sectional views of the 2D crystals (Fig. 3, *bottom*) indicate that the smallest roughness is obtained in the type-3 *P*2 crystal. The surface corrugation amplitude of the type-3 *P*2 crystal was < 1 nm, whereas it was 2–3 nm in the other two crystals. The surface roughness measurements are summarized in Fig.4. For each crystal surface, the root-mean square (RMS) roughness was calculated using corresponding AFM images from which maximum diffraction spots better than 0.67 nm^{-1} were obtained. For a comparison, the values of RMS roughness of glass and mica surfaces are also given in Fig.4. The values of RMS roughness of the type-1 and type-2 *P*2 crystals were comparable to that of bare glass surfaces, while the surface roughness of the type-3 *P*2 crystal was only slightly larger than that measured for atomically flat mica.

High-speed AFM imaging of the crystals also showed a different aspect of the crystals. As found by our previous study with the type-1 *P*2 crystal (25), the diffusion of vacancy defects were also observed in the type-2 *P*2 crystal. In contrast, the vacancies in the type-3 *P*2 crystal did not diffuse, indicating that the intermolecular interactions of streptavidin are considerably stronger in the type-3 *P*2 crystal than those in the other two crystals. In fact, the type-3 *P*2 crystal was highly resistant to an increased tapping force exerted by an oscillating tip. Although the type-1 and type-2 *P*2 crystals are somewhat fragile, we can treat them by glutaraldehyde when higher mechanical strength is required. After the treatment, the crystal surfaces still retain practically strong enough affinity for biotinylated proteins.

Resistance to nonspecific protein adsorption of streptavidin 2D crystals

Resistance of substrate surfaces to nonspecific binding of proteins is important for the immobilized proteins to retain their native activities and also for selectively attaching a specific protein contained in a multi-component sample. Using TIRFM, we examined this issue by measuring nonspecific adsorption of fluorescently labeled CaM to the streptavidin 2D crystals. For the TIRFM measurements, we used coverslips as a substitute for mica.

First, we confirmed that streptavidin can be crystallized on glass-supported lipid bilayers using the same crystallization procedures used for mica. Fig. 5 *A* shows an AFM image of

the type-1 *P*2 crystal formed on a glass-supported lipid bilayer. The type-2 and type-3 *P*2 crystals were also formed. The lattice constants of these crystals were consistent with that formed on mica-supported lipid bilayer. However, the surfaces of the crystals formed on glass-supported lipid bilayers showed slight undulation reflecting the rugged surface of the coverslip underneath the supported lipid bilayer. Next, TIRFM measurements were performed to examine non-specific binding of proteins to the crystal surfaces. A 0.1 nM Cy3-CaM solution was applied to a flow cell, on the surface of which the type-1 *P*2 crystals were formed. After washing the flow cell with buffer A solution, no fluorescent spots were observed (Fig. 5 *B*). When 100-times higher concentration of Cy3-CaM was added without being followed by washing, a low density of fluorescent spots was observed (Fig. 5 *C*). On the other hand, when 0.1 nM biotinylated Cy3-CaM was used, a significant density of fluorescent spots was observed (Fig. 5 *D*). Even when CaM was replaced with bovine serum albumin, we obtained similar results. Thus, the type-1 *P*2 crystal surface is resistant to nonspecific binding to proteins. In addition, the chemical fixation of the type-1 *P*2 crystal with glutaraldehyde had no effects on this resistance. Comparable results were also obtained for the type-2 and type-3 *P*2 crystals although densely packed fluorescent regions were frequently observed for these crystals. Probably, this nonspecific binding is due likely to the partial disruption of lipid bilayer on coverslips under the buffer conditions used for these types of crystals, since examinations by AFM imaging for the type-2 and type-3 *P*2 crystals formed on mica-supported lipid bilayers did not show at all such densely assembled regions of applied proteins (CaM, GroEL, GroES, and actin).

Ca^{2+}-induced conformational change in CaM

As the type-3 *P*2 crystal shows the smallest roughness among the three types of crystals (Fig. 4), it is a suitable substrate when structural changes of relatively small proteins are imaged by AFM. Here, we used CaM (16.7 kDa) as a small protein to be visualized on the type-3 *P*2 crystal. CaM is a Ca^{2+} binding protein with the N-terminal and C-terminal globular domains connected by a central linker helix (33). Each globular domain contains two Ca^{2+} binding sites. CaM undergoes a conformational change upon Ca^{2+} binding (34, 35).

Fig. 6 *A* show successive AFM images captured at 1 s/frame of biotinylated CaM specifically bound to the type-3 *P*2 crystal in the absence of Ca^{2+}. Rather than a pair of two globular domains as expected from earlier structural studies (33, 34), the immobilized CaM was observed as single globes. This probably arises from no immobilization of either of the globular domains because of the low content of biotin (0.6 per molecule) and the intrinsic flexibility of the central linker helix. In fact, “noise” spikes frequently appeared around the globes, indicating rapidly moving moieties around the globes. The addition of Ca^{2+} to the

sample changed the appearance of CaM; larger lateral dimensions and taller height (Fig. 6 *B*). The average height was increased from 1.9 ± 0.3 nm to 2.6 ± 0.4 nm (Fig. 6 *D*), while the average half width was increased from 4.3 ± 1.0 nm to 5.9 ± 1.1 nm. This change in height and width was fully reversible in the same sample (Fig. 6 *C*), representing the conformational change of CaM.

Previous structural studies have indicated that the conformational change of CaM upon binding to Ca^{2+} at each globular domain is drastic (33, 34). The binding of Ca^{2+} induces an opening of the two EF-hand motifs in each globular domain. As a result, the distances between two helices in each EF-hand substantially increase (2.5 – 6.2 Å) upon binding to Ca^{2+}. The increase in the dimension of CaM observed in Fig. 6 *B* is close to the opening of the EF-hands in the immobilized globular domain. This result indicates that AFM measurements on the streptavidin crystal enable the detection of conformational change of the immobilized proteins in the z-dimension at subnanometer precision.

Immobilization of GroEL with controlled orientation

Streptavidin 2D crystals will benefit AFM imaging studies, if the orientation of the immobilized proteins can be controlled. This control can be achieved by the introduction of more than two biotin molecules at specific sites of a protein. Here we immobilized GroEL on the type-1 *P*2 crystal surface in a side-on orientation. GroEL and GroES are chaperonin proteins that assist folding of other proteins in vivo and in vitro (36, 37). GroEL is a cylindrical protein composed of two heptameric rings stacked back to back, each of which is comprised of seven identical ATPase subunits (38). During the ATPase cycle, GroES transiently binds to the ends of the double rings (39, 40).

Previously, the association and dissociation between GroEL and GroES were directly observed by AFM (11, 12). In these studies, GroEL was adsorbed onto a mica surface, in which the GroEL has a strong tendency to take an end-up orientation. In this orientation, only one GroEL ring is exposed to the aqueous buffer and accessible to GroES floating in the solution. To solve this problem, previous TIRFM studies introduced biotin to the Cys-490 residue located at the outer surface of the equatorial domain of the D490C GroEL mutant (41, 42). The resulting biotinylated GroEL is expected to be anchored on a streptavidin layer in a side-on orientation, although any evidence was not provided before.

Fig. 7 shows successive AFM images of the biotinylated GroEL mutant immobilized on the type-1 *P*2 crystal in the presence of GroES and ADP. Two species with different appearances were observed. One exhibited a rectangle shape (Fig. 7, *arrowhead*) (not like a circular shape as has been observed with GroEL on a mica surface), indicating GroEL alone in a side-on orientation, and the other exhibited a bullet shape (Fig. 7, *arrow*), indicating a

1:1 complex of GroEL and GroES (39). Interestingly, the protruded side of the bullet-shaped GroEL is switched (*asterisks*; compare the images in Fig. 7), indicating GroES release from one end of the two rings, which is followed by GroES binding to the other end. This behavior occurred reversibly in the GroEL molecule, although most GroEL molecules were rather stable and did not show such dynamic association/disscoation events during the imaging period. Note that GroES never bound to the streptavidin crystal surface even when its concentration was relatively high. As exemplified here, it is possible to immobilize proteins in a desired orientation by introducing multiple biotins to a protein at designed sites.

Visualization of actin polymerization

Here, we further verified the applicability of the streptavidin 2D crystal surfaces to dynamic AFM imaging by directly observing actin polymerization on the type-2 *P*2 crystal surface. The polymerization of actin is a key process in a variety of cellular functions (43). To date, many studies have demonstrated that the polymerization of actin consists of nucleation and growth steps followed by dynamic equilibrium in the steady state. It is also well known that actin filaments have a structural polarity, so that the polymerization kinetics is different at the two ends of the filaments; the polymerization rate is higher at the barbed end than at the pointed end. Previous TIRFM imaging studies (44, 45) on the polymerization dynamics with individual actin filaments have suggested a polymerization unit not to be monomers alone but an average of monomers, oligomers and fragments. However, analysis of precise molecular events occurring at the filament edges has been difficult due to the limited spatial resolution of optical microscopy. In contrast, high-speed AFM allows direct observation of the polymerization process at the molecular level, thanks to the high spatial resolution and sub-second temporal resolution.

Fig. 8 *A* shows AFM images captured at 0.25 s/frame for a polymerizing actin filament in the presence of non-biotinylated G-actin. Instead of finding actin filament ends, the ends were produced by breaking an actin filament (Fig. 8*A*, *0 s*) by applying an increased tapping force (Fig. 8 *A, 2.0–2.5 s*). This procedure allowed simultaneous visualization of both barbed and pointed ends in the relatively small scan area. The actin filament showed stepwise elongation at one end (Fig. 8 *A*, *arrows* at *6.75 s–13.5 s*, and Fig. 8 *B*), while at the other end, elongation was not observed in the imaging period. From this difference, the end on the left-hand is assigned to be the barbed end. The observed elongation rate at the barbed end was 0.11 μm/min, which is comparable to the values obtained previously (44, 45). Interestingly, a stepwise decrease (3.5 ± 1.4 nm) in the length was occasionally observed (Fig. 8 *B*, *arrows*). An actin filament is composed of two filamentous actin strands organized into an apparent double helix. The actin subunits are spaced 5.5 nm apart along each helix.

The two strands are axially staggered relative to each other by half the subunit repeat (i.e. 2.75 nm). Based on this structure, we can make a correlation between the observed elongation step lengths (Fig. 8 *B*: 3.1 ± 0.9 nm and 5.2 ± 1.1 nm) and the numbers of the molecules incorporated. The smaller step length is close to the half length of an actin subunit, while the larger one well agrees with the size of an actin subunit. The former result indicates monomer binding to the end of one strand that is recessed relative to the end of the other strand. On the other hand, the latter result indicates dimer binding; the barbed end of each strand is bound by an actin subunit, so that the filament elongates by the size of an actin subunit. Therefore, both monomers and dimers are incorporated to the barbed end of actin filaments during the polymerization process.

In a previous TIRFM study on actin polymerization, the polymerization unit was estimated to be six monomers on average (44). This value is significantly larger than that obtained in this study. One possible reason for this discrepancy may be attributed to the annealing of actin fragments, in which fragments associate each other at their ends to form a longer filament. The annealing rate is comparable to the polymerization rate as reported previously (46). Therefore, annealing events will make the apparent polymerization unit larger. We did not observe the annealing process in this study. A further examination of actin polymerization by high-speed AFM will provide deeper insights into the actin polymerization process.

CONCLUSION

The characterization of the three types of streptavidin 2D crystals showed their appropriate properties as substrates to which proteins are immobilized for dynamic AFM imaging, i.e., uniformity over relatively wide areas, small roughness and resistance to nonspecific binding to proteins. Among the three types of crystals, the type-3 *P*2 crystal seems the most appropriate choice for a wide range of biological samples because of the smallest roughness and the highest stability (glutaraldehyde treatment is unnecessary) Although type-3 *P*2 crystal often contains line cracks, they are also resistant to nonspecific binding to proteins because their surfaces are those of lipid bilayers. When the presence of line cracks is undesired in dynamic AFM imaging of a biological sample, we can use the type-1 or type-2 *P*2 crystals of which surfaces have high uniformity over a wide area. The stable immobilization of oligomerized proteins such as GroEL and actin filaments to the surfaces can be achieved easily by introducing multiple biotin molecules. The ability of the crystal surfaces to specifically bind to biotinylated proteins (or his-tag conjugated proteins) without nonspecific binding to proteins allows studying dynamic interaction processes between protein molecules, as demonstrated here in the observation of GroES-GroEL

binding and actin polymerization.

SUPPORTING MATERIAL
A movie is available at
www.biophys.org/biophysj/supplemental/S0006-3495(XX)XXXXX-X.

Acknowledgement

This work was supported by the CREST project and the project of Development of System and Technology for Advanced Measurement and Analysis (JST, Japan), and a Grant-in-Aid for Basic Research (S) (No. 20221006; JSPS, Japan).

REFERENCES

1. Binnig, G., C. F. Quate, and C. Gerber. 1986. Atomic force microscope. Phys. Rev. Lett. 56:930–933.

2. Mou, J., D. M. Czajkowsky, S. Sheng, R. Ho, and Z. Shao. 1996. High resolution surface structure of *E. coli* GroES oligomer by atomic force microscopy. FEBS Lett. 381:161–164.

3. Müller, D. J., H. J. Sass, S. A. Müller, G. Büldt, and A. Engel. 1999. Surface structures of native bacteriorhodopsin depend on the molecular packing arrangement in the membrane. J. Mol. Biol. 285:1903–1909.

4. Scheuring, S., J. Seguin, S. Marco, D. Lévy, B. Robert, and J. L. Rigaud. 2003. Nanodissection and high-resolution imaging of the *Rhodopseudomonas viridis* photosynthetic core complex in native membranes by AFM. Proc. Natl. Acad. Sci. USA. 100:1690–1693.

5. Lyubchenko, Y., L. Shlyakhtenko, R. Harrington, P. Oden, and S. Lindsay. 1993. Atomic force microscopy of long DNA: Imaging in air and under water. Proc. Natl. Acad. Sci. USA. 90:2137–2140.

6. Thomson, N. H., B. L. Smith, N. Almqvist, L. Schmitt, M. Kashlev, E. T. Kool, and P. K. Hansma. 1999. Oriented, active *Escherichia coli* RNA polymerase: An atomic force microscope study. Biophys. J. 76:1024–1033.

7. El Kirat, K., I. Burton, V. Dupres, and Y. F. Dufrene. 2005. Sample preparation procedures for biological atomic force microscopy. J. Microsc. 218:199–207.

8. Karrasch, S., M. Dolder, F. Schabert, J. Ramsden, and A. Engel. 1993. Covalent binding of biological samples to solid supports for scanning probe microscopy in buffer solution. Biophys. J. 65:2437–2446.

9. Wagner, P., M. Hegner, P. Kernen, F. Zaugg, and G. Semenza. 1996. Covalent immobilization of native biomolecules onto Au(111) via *N*-hydroxysuccinimide ester functionalized self-assembled monolayers for scanning probe microscopy. Biophys. J.

70:2052–2066.
10. Kasas, S., N. H. Thomson, B. L. Smith, H. G. Hansma, X. Zhu, M. Guthold, C. Bustamante, E. T. Kool, M. Kashlev, and P. K. Hansma. 1997. *Escherichia coli* RNA polymerase activity observed using atomic force microscopy. Biochemistry. 36:461–468.
11. Viani, M. B., L. I. Pietrasanta, J. B. Thompson, A. Chand, I. C. Gebeshuber, J. H. Kindt, M. Richter, H. G. Hansma, and P. K. Hansma. 2000. Probing protein–protein interactions in real time. Nat. Struct. Biol. 7:644–647.
12. Yokokawa, M., C. Wada, T. Ando, N. Sakai, A. Yagi, S. H. Yoshimura, and K. Takeyasu. 2006. Fast-scanning atomic force microscopy reveals the ATP/ADP-dependent conformational changes of GroEL. EMBO J. 25:4567–4576.
13. Müller, D. J., and A. Engel. 1999. Voltage and pH-induced channel closure of porin OmpF visualized by atomic force microscopy. J. Mol. Biol. 285:1347–1351.
14. Ando, T., N. Kodera, E. Takai, D. Maruyama, K. Saito, and A. Toda. 2001. A high-speed atomic force microscope for studying biological macromolecules. Proc. Natl. Acad. Sci. USA. 98:12468–12472.
15. Ando, T., T. Uchihashi, and T. Fukuma. 2008. High-speed atomic force microscopy for nano-visualization of dynamic biomolecular processes. Prog. Surf. Sci. 83:337–437.
16. Scheuring, S., D. J. Müller, P. Ringler, J. B. Heymann, and A. Engel. 1999. Imaging streptavidin 2D crystals on biotinylated lipid monolayers at high resolution with the atomic force microscope. J. Microsc. 193:28-35.
17. Blankenburg, R., P. Meller, H. Ringsdorf, and C. Salesse. 1989. Interaction between biotin lipids and streptavidin in monolayers: Formation of oriented two-dimensional protein domains induced by surface recognition. Biochemistry. 28:8214–8221.
18. Darst, S. A., M. Ahlers, P. H. Meller, E. W. Kubalek, R. Blankenburg, H. O. Ribi, H. Ringsdorf, and R. D. Kornberg. 1991. Two-dimensional crystals of streptavidin on biotinylated lipid layers and their interactions with biotinylated macromolecules. Biophys. J. 59:387–396.
19. Calvert, T. L., and D. Leckband. 1997. Two-dimensional protein crystallization at solid-liquid interfaces. Langmuir. 13:6737–6745.
20. Reviakine, I., and A. Brisson. 2001. Streptavidin 2D crystals on supported phospholipid bilayers: Toward constructing anchored phospholipid bilayers. Langmuir. 17:8293–8299.
21. Green, N. M. 1990. Avidin and streptavidin. Methods Enzymol. 184:51–67.
22. Heyes, C. D., A. Y. Kobitski, E. V. Amirgoulova, and G. U. Nienhaus. 2004. Biocompatible surfaces for specific tethering of individual protein molecules. J. Phys. Chem. B. 108:13387–13394.
23. Wang, S. W., C. R. Robertson, and A. P. Gast. 1999. Molecular arrangement in

two-dimensional streptavidin crystals. Langmuir. 15:1541–1548.
24. Ratanabanangkoon, P., and A. P. Gast. 2003. Effect of ionic strength on two-dimensional streptavidin crystallization. Langmuir. 19:1794–1801.
25. Yamamoto, D., T. Uchihashi, N. Kodera, and T. Ando. 2008. Anisotropic diffusion of point defects in a two-dimensional crystal of streptavidin observed by high-speed atomic force microscopy. Nanotechnology. 19:384009(9pp).
26. Koide, H., T. Kinoshita, Y. Tanaka, S. Tanaka, N. Nagura, G. Meyer zu Hörste, A. Miyagi, and T. Ando. 2006. Identification of the single specific IQ motif of myosin V from which calmodulin dissociates in the presence of Ca^{2+}. Biochemistry. 45:11598–11604.
27. Kunioka, Y., and T. Ando. 1996. Innocuous labeling of the subfragment-2 region of skeletal muscle heavy meromyosin with a fluorescent polyacrylamide nanobead and visualization of individual heavy meromyosin molecules. J. Biochem. 119:1024–1032.
28. Taniguchi, M., T. Yoshimi, K. Hongo, T. Mizobata, and Y. Kawata. 2004. Stopped-flow fluorescence analysis of the conformational changes in the GroEL apical domain: Relationships between movements in the apical domain and the quaternary structure of GroEL. J. Biol. Chem. 279:16368–16376.
29. Sakamoto, T., I. Amitani, E. Yokota, and T. Ando. 2000. Direct observation of processive movement by individual myosin V molecules. Biochem. Biophys. Res. Commun. 272:586–590.
30. Wang, S. W., C. L. Poglitsch, M. T. Yatcilla, C. R. Robertson, and A. P. Gast. 1997. Solid phase coexistence in chiral domains of two-dimensional streptavidin crystals. Langmuir. 13:5794–5798.
31. Hemming, S. A., A. Bochkarev, S. A. Darst, R. D. Kornberg, P. Ala, D. S. C. Yang, and A. M. Edwards. 1995. The mechanism of protein crystal growth from lipid layers. J. Mol. Biol. 246:308–316.
32. Fechner, P., T. Boudier, S. Mangenot, S. Jaroslawski, J. N. Sturgis, and S. Scheuring. 2009. Structural information, resolution, and noise in high-resolution atomic force microscopy Topographs. Biophys. J. 96:3822–3831.
33. Babu, Y. S., C. E. Bugg, and W. J. Cook. 1988. Structure of calmodulin refined at 2.2 Å resolution. J. Mol. Biol. 204:191–204.
34. Zhang, M., T. Tanaka, and M. Ikura. 1995. Calcium-induced conformational transition revealed by the solution structure of apo calmodulin. Nat. Struct. Biol. 2:758–767.
35. Ikura, M. 1996. Calcium binding and conformational response in EF-hand proteins. Trends Biochem. Sci. 21:14–17.
36. Bukau, B., and A. L. Horwich. 1998. The Hsp70 and Hsp60 chaperone machines. Cell. 92:351–366.

37. Hartl, F. U., and M. Hayer-Hartl. 2002. Molecular chaperones in the cytosol: from nascent chain to folded protein. Science. 295:1852–1858.
38. Braig, K., Z. Otwinowski, R. Hegde, D. C. Boisvert, A. Joachimiak, A. L. Horwich, and P. B. Sigler. 1994. The crystal structure of the bacterial chaperonin GroEL at 2.8 Å Nature. 31:578–586.
39. Xu, Z., A. L. Horwich, and P. B. Sigler. 1997. The crystal structure of the asymmetric GroEL-GroES-$(ADP)_7$ chaperonin complex. Nature. 388:741–750.
40. Horwich, A. L., W. A. Fenton, E. Chapman, and G. W. Farr. 2007. Two families of chaperonin: Physiology and mechanism. Annu. Rev. Cell Dev. Biol. 23:115-145.
41. Taguchi, H., T. Ueno, H. Tadakuma, M. Yoshida, and T. Funatsu. 2001. Single-molecule observation of protein–protein interactions in the chaperonin system. Nat. Biotechnol. 19:861–865.
42. Ueno, T., H. Taguchi, H. Tadakuma, M. Yoshida, and T. Funatsu. 2004. GroEL mediates protein folding with a two successive timer mechanism. Mol. Cell. 14:423–434.
43. Pollard, T. D., and G. G. Borisy. 2003. Cellular motility driven by assembly and disassembly of actin filaments. Cell. 112:453–465.
44. Fujiwara, I., S. Takahashi, H. Tadakuma, T. Funatsu, and S. Ishiwata. 2002. Microscopic analysis of polymerization dynamics with individual actin filaments. Nat. Cell Biol. 4:666–673.
45. Kuhn, J. R., and T. D. Pollard. 2005. Real-time measurements of actin filament polymerization by total internal reflection fluorescence microscopy. Biophys. J. 88:1387–1402.
46. Murphy, D. B., R. O. Gray, W. A. Grasser, and T. D. Pollard. 1988. Direct demonstration of actin filament annealing in vitro. J. Cell Biol. 106:1947–1954.

Figure Legends

FIGURE 1 Low magnification AFM images of streptavidin 2D crystals formed on mica-supported lipid bilayer. The space group symmetries of the crystals are (*A*) type-1 *P*2, (*B*) type-2 *P*2 and (*C*) type-3 *P*2. The arrows indicate large particles found on the streptavidin 2D crystals. The asterisk in (*B*) indicates a non-crystallized region. The arrowheads in (*C*) indicate cracks found on the type-3 *P*2 crystal. These AFM images were obtained at a scan rate of 1 s/line (512 pixels). Z-scale: 5 nm.

FIGURE 2 Medium magnification AFM images of streptavidin 2D crystals formed on mica-supported lipid bilayer. The space group symmetries of the crystals are (*A*) type-1 *P*2, (*B*) type-2 *P*2 and (*C*) type-3 *P*2. The arrowheads indicate vacancies. The dashed line in (*C*) outlines a line defect. The arrows indicate small particles. These AFM images were obtained at a scan rate of 1 s/line (512 pixels). Z-scale: 3.5 nm.

FIGURE 3 High magnification surface topographies of the streptavidin 2D crystals formed on mica-supported lipid bilayer. The space group symmetries of the crystals are (*A*) type-1 *P*2, (*B*) type-2 *P*2 and (*C*) type-3 *P*2. (*Top*); AFM images of the streptavidin 2D crystals. These AFM images were obtained at an imaging rate of 1 s/frame with 256×256 pixels. (*Middle*); Calculated diffraction patterns from the AFM images shown in the *top* panels. The large circles indicate the position of 1 nm^{-1}. The small circles surround diffraction spots with the apparent highest resolution detected. In the reciprocal lattice, the diffraction spots can be discerned up to (5, –1) for the type-1 *P*2, (4, 4) for the type-2 *P*2 and (3, –4) for the type-3 *P*2, corresponding to the apparent resolutions of 1.14, 1.19 and 1.17 nm, respectively. Note that these values do not necessarily represent the spatial resolution of the images because of a tip effect (32). (*Bottom*); Cross sections of the surface profiles along the lines indicated in the AFM images in the *top* panels.

FIGURE 4 RMS surfaces roughness of glass, mica and streptavidin 2D crystals (type-1, type-2 and type-3) formed on mica-supported lipid bilayer. The data were obtained from several high magnification AFM images (scanning area of 75 × 75 nm^2) of respective surfaces. The error bars are SD.

FIGURE 5 Specific and nonspecific adsorption of CaM to the type-1 *P*2 crystal of streptavidin formed on glass surface. (*A*) AFM image of the type-1 *P*2 crystal formed on a glass surface. The AFM image was obtained at an imaging rate of 1 s/frame with 256×256 pixels. Z-scale: 3.3 nm. (*B–D*) TIRFM images of Cy3-CaM attached onto the type-1 *P*2

crystal of streptavidin. (*B*) After incubating in the presence of 0.1 nM Cy3-CaM for 3 min, the flow cell was washed with buffer A. (*C*) The flow cell was incubated in the presence of 10 nM Cy3-CaM without being followed by washing out free Cy3-CaM. (*D*) Specific binding of biotinylated Cy3-CaM after the incubation in the presence of 0.1 nM bitinylated Cy3-CaM for 3 min.

FIGURE 6 Biotinylated CaM immobilized on the type-3 *P*2 crystal of streptavidin. The successive AFM images were obtained in the absence (*A*, *C*) or presence (*B*) of Ca^{2+}, at an imaging rate of 1 s/frame with 256×256 pixels. Z-scale: 6 nm. The three sets of imaging for the same sample were performed in the alphabetical order. Before taking images of (B) and (C), the buffer solution was replaced with 2 mM Ca^{2+}-containing buffer-A and buffer-A, respectively. Numbers in the AFM images indicate frame numbers. (*D*) Histogram of the height of the immobilized CaM in the presence or absence of Ca^{2+}.

FIGURE 7 AFM images of GroEL alone and GroEL-GroES complex. The GroEL is D490C mutant, the Cys-490 residues of which are labeled with biotin, and is immobilized in a side-on orientation on the streptavidin type-1 *P*2 crystal that is chemically fixed with glutaraldehyde. The arrowhead indicates GroEL alone and the arrow indicates the GroEL-GroES complex. The dashed lines indicate the end positions of the GroEL. The asterisks indicate GroES bound to one of the GroEL rings. The AFM images were obtained at an imaging rate of 2 s/frame with 200×200 pixels. Z-scale: 19 nm. Numbers in the AFM images indicate frame numbers.

FIGURE 8 Polymerization process at actin filament ends observed by high-speed AFM. (*A*) High-speed AFM images of partially biotinylated actin filaments on the streptavidin type-2 *P*2 crystal that is chemically fixed with glutaraldehyde. The dashed lines and dot-dash lines indicate the initial positions of the barbed and pointed ends, respectively. The ends were produced by partially dissecting the filament by an oscillating cantilever tip. The arrows indicate the positions of the growing barbed end of the dissected actin filament. The successive images were obtained at an imaging rate of 0.25 s/frame with 256×128 pixels. Z-scale: 11 nm. (*B*) Change with time elapse in the barbed end position along the longitudinal axis of the filament. The position was measured from the successive AFM images. The arrows indicate decrease in the length of the filament.

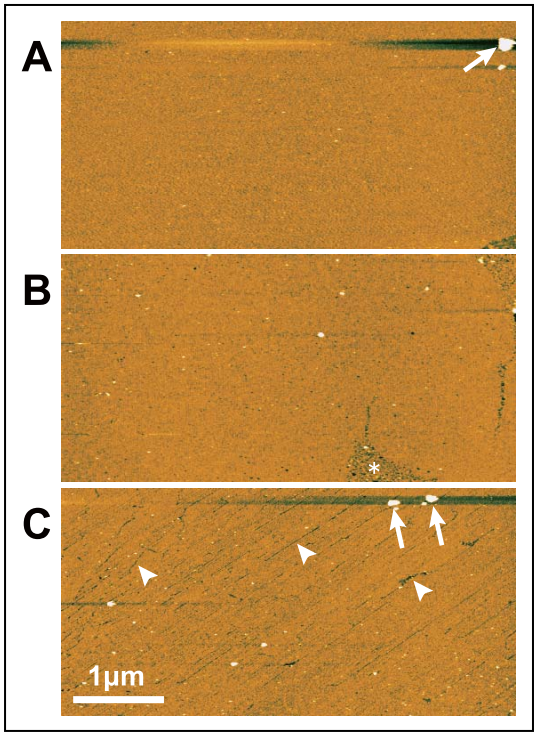

Fig. 1

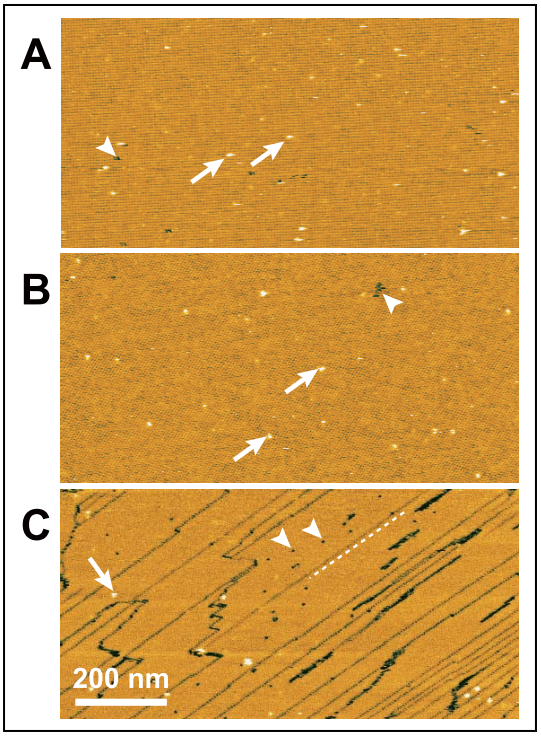

Fig. 2

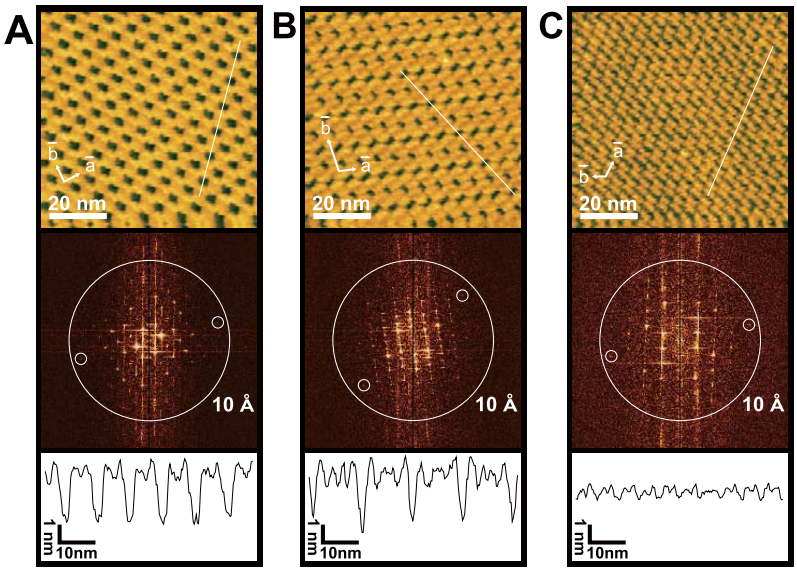
A
B
C
20 nm
20 nm
20 nm
10 Å
10 Å
10 Å
10nm
10nm
10nm

Fig. 3

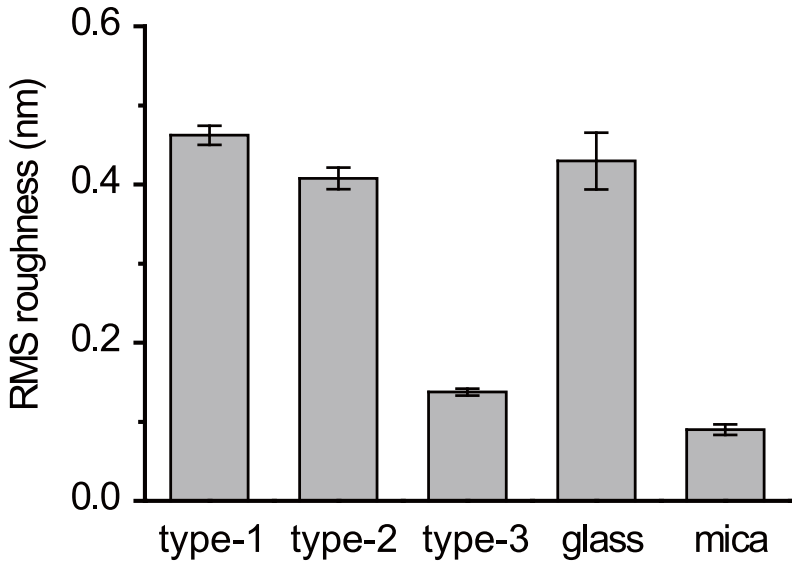
RMS roughness (nm)
0.6
0.4
0.2
0.0
type-1
type-2
type-3
glass
mica

Fig. 4

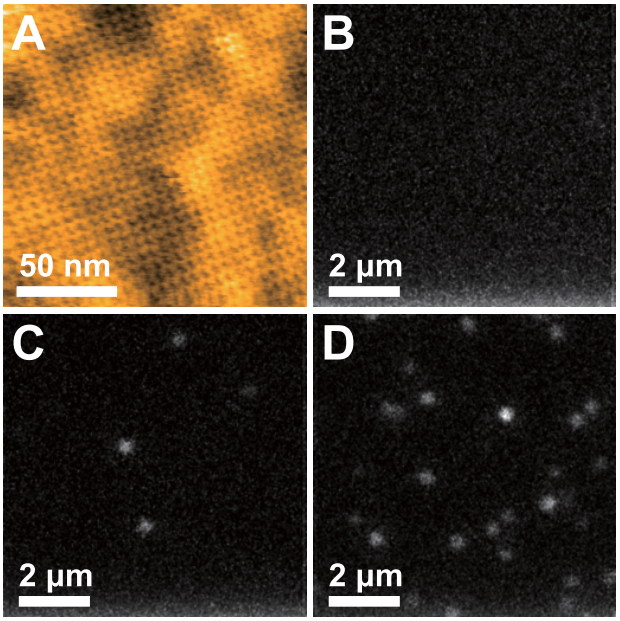
A
50 nm
B
2 µm
C
2 µm
D
2 µm

Fig. 5

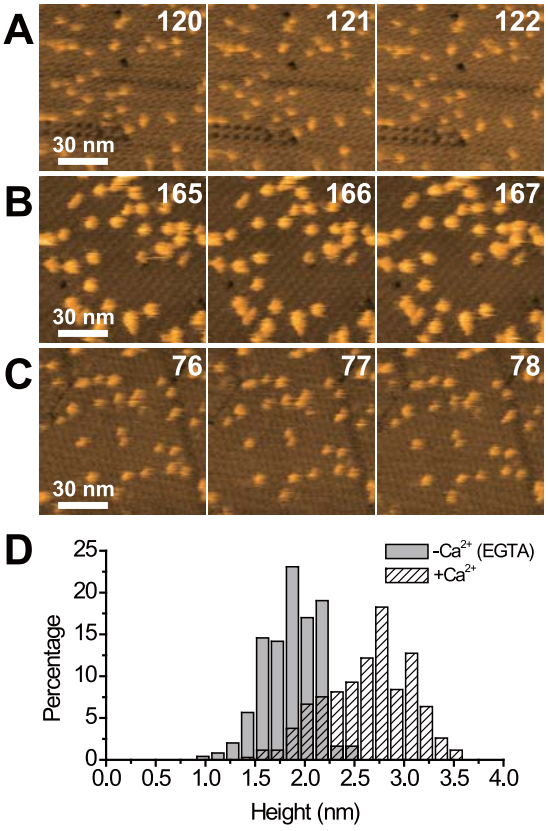
A
120
121
122
30 nm
B
165
166
167
30 nm
C
76
77
78
30 nm
D
-Ca2+ (EGTA)
+Ca2+
Percentage
25
20
15
10
5
0
0.0
0.5
1.0
1.5
2.0
2.5
3.0
3.5
4.0
Height (nm)

Fig. 6

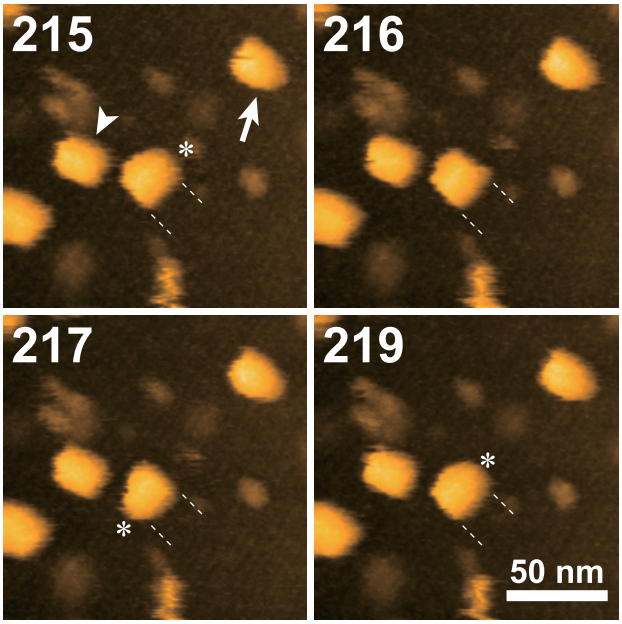
215
216
217
219
50 nm

Fig. 7

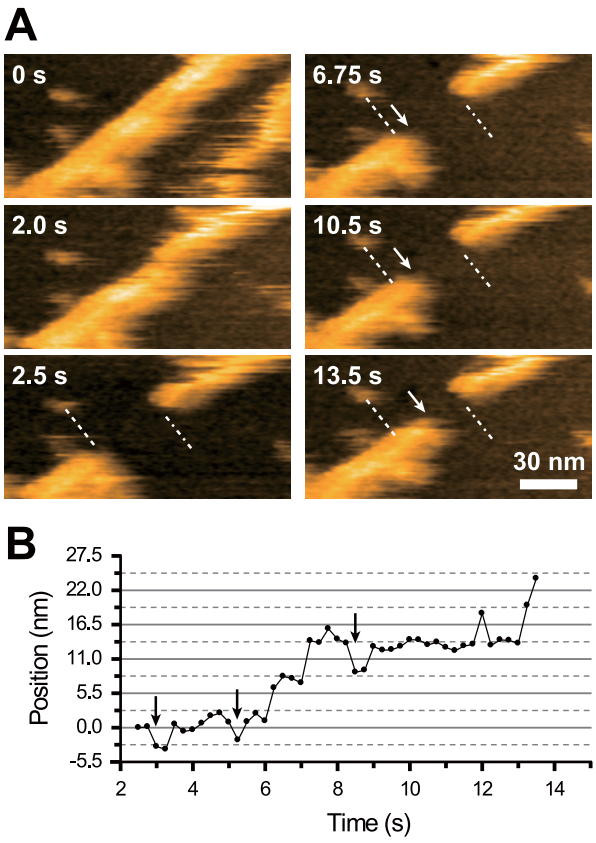
A
0 s
6.75 s
2.0 s
10.5 s
2.5 s
13.5 s
30 nm
B
Position (nm)
27.5
22.0
16.5
11.0
5.5
0.0
-5.5
2
4
6
8
10
12
14
Time (s)

Fig. 8